Volume 92, March/April 2022

ELSEVIER

European Journal of Mechanics

B/Fluids

(Founded in 1961 as Journal de Mécanique)

www.elsevier.com/locate/ejmflu

EUROPEAN JOURNAL OF MECHANICS
B/FLUIDS

An official medium of publication for EUROMECH – 'European Mechanics Society'

The manuscripts should be sent to one of the Editors-in-Chief

European Journal of Mechanics, B/Fluids

COUNTRY

Netherlands

Universities and research institutions in Netherlands

SUBJECT AREA AND CATEGORY

Mathematics
Mathematical Physics

Physics and Astronomy
Physics and Astronomy (miscellaneous)

PUBLISHER

Elsevier BV

H-INDEX

69

PUBLICATION TYPE

Journals

ISSN

09977546

COVERAGE

1990-1992, 1995-2021

INFORMATION

Homepage

How to publish in this journal

Contact

SCOPE

The European Journal of Mechanics - B/Fluids publishes papers in all fields of fluid mechanics. Although investigations in well-established areas are within the scope of the journal, recent developments and innovative ideas are particularly welcome. Theoretical, computational and experimental papers are equally welcome. Mathematical methods, be they deterministic or stochastic, analytical or numerical, will be accepted provided they serve to clarify some identifiable problems in fluid mechanics, and provided the significance of results is explained. Similarly, experimental papers must add physical insight in to the understanding of fluid mechanics.

FIND SIMILAR JOURNALS

1	2	3	4
Fluid Dynamics Research	**Theoretical and Computational Fluid**	**International Journal of Heat and Fluid Flow**	**Physics of Fluids**
GBR	USA	NLD	USA
83% similarity	**82%** similarity	**73%** similarity	**69%** simila

SJR

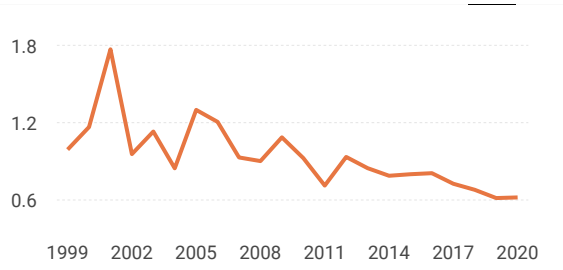

Total Documents

Total Cites Self-Cites

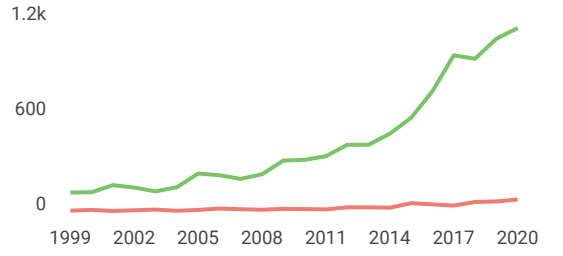

External Cites per Doc Cites per Doc

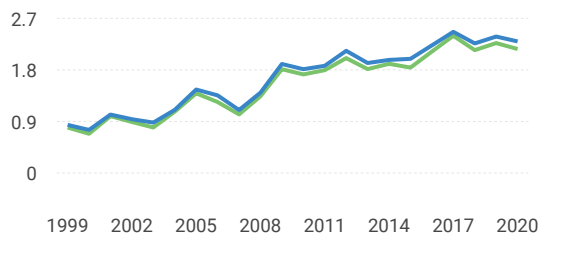

Citations per document

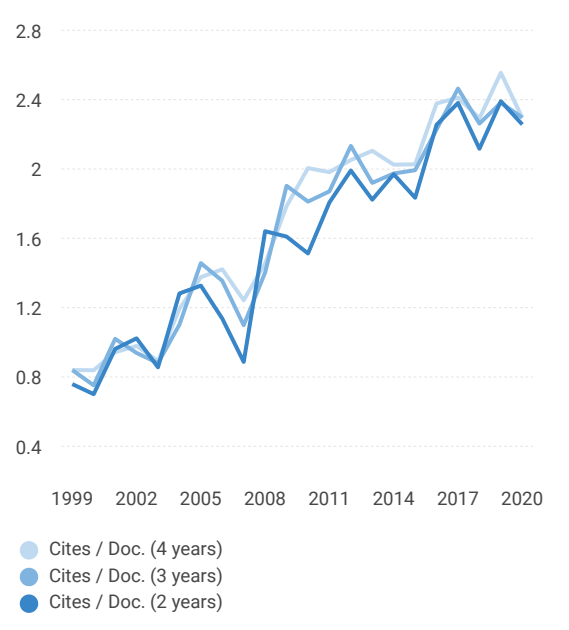

% International Collaboration

Citable documents Non-citable documents

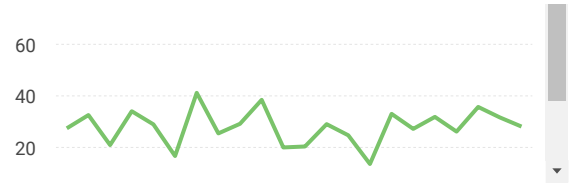

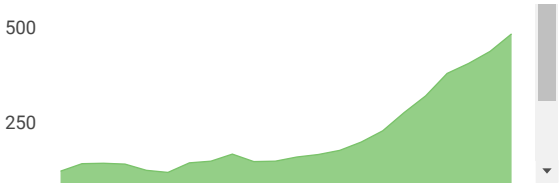

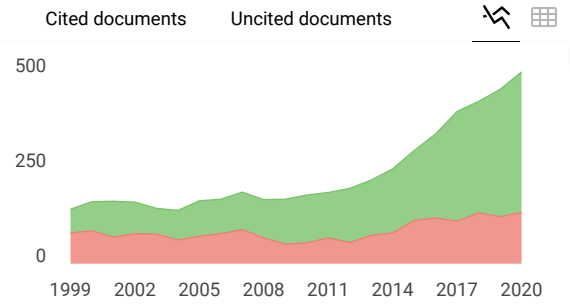

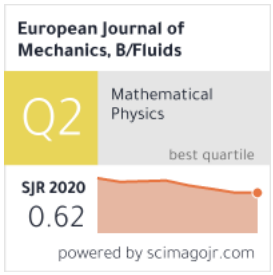

← Show this widget in your own website

Just copy the code below and paste within your html code:

<a href="https://www.scimag

SCImago Graphica

Explore, visually communicate and make sense of data with our **new free tool**.

Get it

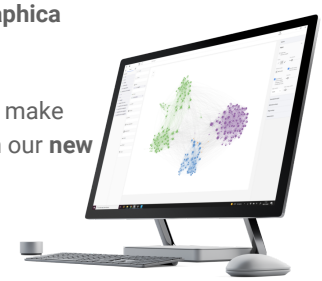

Metrics based on Scopus® data as of April 2021

Leave a comment

Name

Email
(will not be published)

I'm not a robot
reCAPTCHA
Privacy - Terms

Submit

The users of Scimago Journal & Country Rank have the possibility to dialogue through comments linked to a specific journal. The purpose is to have a forum in which general doubts about the processes of publication in the journal, experiences and other issues derived from the publication of papers are resolved. For topics on particular articles, maintain the dialogue through the usual channels with your editor.

European Journal of Mechanics / B Fluids 85 (2021) 276–288

Contents lists available at ScienceDirect

European Journal of Mechanics / B Fluids

journal homepage: www.elsevier.com/locate/ejmflu

Lattice Boltzmann simulation of the Rayleigh–Taylor Instability (RTI) during the mixing of the immiscible fluids

Kumara Ari Yuana [a,b], Bahrul Jalaali [c], Eko Prasetya Budiana [a,d], Pranowo [e], Adhika Widyaparaga [a,f], Indarto [a,f], Deendarlianto [a,f,*]

[a] Department of Mechanical and Industrial Engineering, Faculty of Engineering, Universitas Gadjah Mada, Jalan Grafika No. 2, Yogyakarta 55281, Indonesia
[b] Department of Informatics, Faculty of Computer Science, Universitas Amikom Yogyakarta, Jl Ringroad Utara, Condongcatur, Sleman, Yogyakarta, Indonesia
[c] Department of Mechanical Engineering, Sekolah Tinggi Teknik Adisutjipto, Jl. Janti Blok R Lanud, Yogyakarta, 55198, Indonesia
[d] Department of Mechanical Engineering, Faculty of Engineering, Universitas Sebelas Maret, Jalan Ir. Sutami No. 36A, Surakarta 57126, Indonesia
[e] Department of Informatics, Faculty of Engineering, Universitas Atma Jaya Yogyakarta, Jalan Babarsari No. 44, Yogyakarta 55281, Indonesia
[f] Center for Energy Studies, Universitas Gadjah Mada, Sekip K-1A Kampus UGM, Yogyakarta 55281, Indonesia

ARTICLE INFO

Article history:
Received 8 June 2020
Received in revised form 23 August 2020
Accepted 13 October 2020
Available online 15 October 2020

Keywords:
Raleigh–Taylor instability
Lattice Boltzmann Method
Equation of state (EOS)
Bubble and spike

ABSTRACT

The Lattice Boltzmann Method (LBM) was implemented to simulate the two-dimensional (2-D) Rayleigh–Taylor instability (RTI) during the mixing of the immiscible fluids. Two important parameters of the density and the viscosity as represented respectively by the Atwood and the Reynolds numbers were considered. In the calculation the density of two immiscible fluids was calculated by using the equation of state (EOS). In the present simulations, both Atwood and Reynolds numbers were varied in order to investigate the time variations of the interfacial behavior during RTI, the position of bubbles and spikes, and the horizontal average density. The results indicate that the Atwood number has a higher effect than the Reynolds number in the mixing process during RTI. The bubbles and spikes positions go farther in the displacement with the increase of both Reynolds and Atwood numbers. Moreover, the increase of both Reynolds and Atwood numbers accelerate the mixing process during RTI.

1. Introduction

The Raleigh–Taylor instability (RTI) can be found in engineering applications such as boiling and heat exchanger facilities [1]. In pool boiling regime, low density vapor at the lower part props-up the liquid phase. Due to the gravity, the liquid-phase descends through the vapor phase to contact the hot surface. Consequently, the liquid will evaporate into the lower density fluid as the vapor. Moreover, the latent heat transfer occurs during this phenomenon. The overall phenomena mean that more effective heat transfer exists during the boiling regimes. For the comprehensive understanding of the latest state of the art of RTI the readers may refer to [1] and [2].

The main issues of the RTI are: (1) the physical understanding of the flows due to the hydrodynamic instabilities, (2) the flow structure during the hydrodynamic instabilities, and (3) the effect of the initial perturbations on the flows during RTI. The induced flows due to the RTI can be explained in the stages from linear, nonlinear, and transitions to turbulence flows. The linear stage occurs when the position and the velocity are related linearly. The nonlinear stage occurs if both the position and the velocity have a non-linearly relationship. Beyond the linear and the non-linear stages, a transition to turbulence can be found, whereas the problem deals with the uncertainty of the hydrodynamic behavior [3].

The experimental investigations of RTI during the film boiling were investigated by Seo and Bang (2015) [4]. During the film boiling, the film vapor, which has a lower density at lower position, supports the higher density (liquid). The RTI phenomenon exists when the film vapor penetrates into the liquid, in which at the same time the liquid descends and contacts the hot surface. Immediately after the liquid contacts the hot surface, the liquid turns into the vapor. From the heat transfer point of view, it produces a high heat transfer process due to both latent and sensible temperature drop. In their experiment, the effects of the surface diameter of the heater cylinder and the system pressure on RTI were examined. The investigated parameter was the distance between the perturbations that was defined as the wavelength

* Correspondence to: Department of Mechanical & Industrial Engineering, Faculty of Engineering, Universitas Gadjah Mada, Indonesia.
E-mail address: deendarlianto@ugm.ac.id (Deendarlianto).

https://doi.org/10.1016/j.euromechflu.2020.10.006
0997-7546/

that supported the RTI system. The results suggested that the RTI was affected by the wavelength of the corresponding surface coating [4].

The study of RTI on the basis of Navier–Stokes in a complex system by using the finite element numerical method can be found in [5–8]. The Navier–Stokes simulation by using the finite-different method can be also found in [9–15]. A numerical study of RTI by using the combination of the Navier–Stokes equations with the phase field and the diffuse approximate method was carried-out by Talat et al. [16]. They used the meshless solution procedure as a tool to handle the moving boundary problems in the single domain fixed node. In their work, the Atwood numbers ranged from 0.1 to 0.5. Here Atwood number is defined as the ratio between the density difference of the two-fluid system and the mixture density of the two-fluid system. Their result indicated that the effects of Atwood number were mentioned qualitatively, whereas the higher the density ratio of the system, the faster the penetration of spikes and bubbles.

The measurements in the mixing research have become a strong attention for the study of the RTI and Richtmyer–Meshkov instability (RMI). Two conventional parameters of mixing measurement are the ratio of the mixing length to entrainment length and reaction rate of two fluids component. Moreover, the parameter of direct mixing measurement was also proposed by Zhou et al. (2016) [17] in the form of the normalized mixed mass. The advantages of this normalized form are more sensitive for the change of Atwood number and more consistent for both RTI and RMI. Its sensitive was well-posed by Zhou et al. especially under Atwood number of 0.8. That is the increase of Atwood number will decrease the mixing mass at late time for both RTI and RMI [17].

As an alternative method to the conventional Navier–Stokes based computational fluid dynamics (CFD) method, the Lattice Boltzmann Method (LBM) becomes a promising tool for the mathematics modeling and simulation. The LBM is built from the mesoscopic kinetic molecular interactions. It is derived from a more fundamental paradigm rather than the conventional continuum approach. Here, it is not necessarily to solve the Poisson equation (which is computationally expensive), but the pressure can be calculated through the equations of state (EOS). Moreover, LBM is easy to parallelize due to the locality in computation. Finally, the no-slip boundary condition can be handled easily by using a bounce-back scheme [18,19].

The numerical simulations on the effects of the viscosity and the density ratio during the RTI by using LBM were also investigated in the past [20,21]. He et al. (1999) [22] studied the three-dimensional (3-D) structure evolution of the interface by using LBM. Under the condition of the Atwood number of 0.5 and Reynolds number of 1024, the spikes, bubbles and saddle positions were shown. The investigation used the mixed density to quantify of the complex structure during the RTI development [22]. A mixed density of the high and low densities of fluids was studied by the averaging of both densities under the RTI of the density mushy region generation. The mathematical modeling was studied under the assumption of low Atwood number, and under the certain values both of gravity and viscosity. It was shown that there was a similarity between the mushy region that appears after the averaging and the perturbed unstable jump [23]. In the case of two-dimensional (2-D), He et al. (1999) [24] also studied the effect of Reynolds number under a constant Atwood number. The results showed that the viscosity has a little effect on the growth of bubble and spike, but has a significant effect on the development of Kelvin–Helmholtz instability [24].

From the previous studies, it is noticed that the physical properties such as viscosity and density have a strong effect on the RTI. Many studies also explained also the relationship between the physical properties and the development of RTI (e.g. [1–3,17,22,25–30]). Here it is considered that the Atwood number is the important parameter in regards with anisotropy [25]. In general, the ratio of traveled-distance of spike to bubble is always greater than unity. It means that the spike always traveled farther than bubble all the time. There is an anomaly behavior was reported by Zhou & Cabot (2019) [25] for At = 0.8 whereas at late time after the ratio equal to 1.45 for quite long time then was plunged to 1.3. The thresholds of large Atwood number that has the anomaly behavior is indicated at Atwood number greater than 0.75. This behavior encourages lot of opportunities for the investigations of the numerical simulations in this topic. However, a detailed physical mechanism during RTI due to the variations of the density and the viscosity are rare in open literature. Geun & Kim, (2013) [29] performed a numerical study on the interfacial behavior during RTI by varying Reynolds and Atwood numbers. Meanwhile, their conclusion only described that the Atwood number is more influential than the Reynolds number without any quantitative explanations. Therefore, further investigations on the effects of Atwood and Reynolds number on RTI should be carried out more quantitatively by considering the growth of the instability.

The objective of the present work is to investigate the influences of the physical properties in the term of the Atwood number and Reynolds number during RTI in 2-D, numerically. The critical discussions of 2-D in regards with inertial confinement fusion (ICF) and supernovae [31] will discuss as the future challenge of 3-D simulation at the last part of the discussion of the present manuscript. The characteristics of hydrodynamic flow are presented in the form of three plots. Those are the interfacial shape, the positions of bubbles-spikes, and the average density process. Those results then are used to analyze the role of both the Atwood and Reynolds numbers during the RTI.

The present manuscript is organized as follows. First, numerical modeling of LBM is explained. Next, the validations of the numerical result will be presented. The first validation is a comparison between the obtained results from the present study with those of the other numerical schemes. The second validation is a comparison to the experimental results from the previous investigations. Finally, the dependency of Atwood and Reynolds number during RTI will be analyzed.

2. Governing equations and numerical modeling

Two distributions functions are used in the present LBM simulation as also conducted by He et al. (1999) [24]. Those are the distribution function to represent the hydrodynamics fluid flow, and the index function for the interface tracking by using different density distribution. The distribution functions satisfy:

$$g_i(\mathbf{x}+\mathbf{e}_i\Delta t, t+\Delta t) = g_i(\mathbf{x},t) - \frac{1}{\tau_1}(g_i(\mathbf{x},t) - g_i^{eq}(\mathbf{x},t)) + S_i(\mathbf{x},t)\Delta t \quad (1)$$

$$f_i(\mathbf{x}+\mathbf{e}_i\Delta t, t+\Delta t) = f_i(\mathbf{x},t) - \frac{1}{\tau_2}(f_i(\mathbf{x},t) - f_i^{eq}(\mathbf{x},t)) + S_i'(\mathbf{x},t)\Delta t \quad (2)$$

where $f_i(\mathbf{x}, t)$ is the density distribution function in the ith velocity direction at position $\mathbf{x}$ and time step t. The relaxation time, τ_1, relates to the kinematic viscosity of $\upsilon = {c_s}^2(\tau_1 - 0.5)\Delta t$. The relaxation time τ_2 relates to the mobility in the Cahn–Hilliard equation. $S_i(\mathbf{x}, t)\Delta t$ and $S_i'(\mathbf{x}, t)\Delta t$ are the source terms. The equilibrium distributions $g_i^{eq}(\mathbf{x}, t)$ and $f_i^{eq}(\mathbf{x}, t)$ are expressed as follows:

$$g_i^{eq}(\mathbf{x},t) = w_i\left[p + c_s^2\rho\left(\frac{e_{i\alpha}u_\alpha}{c_s^2} + \frac{e_{i\alpha}u_\alpha e_{i\beta}u_\beta}{2c_s^4} - \frac{u_\alpha u_\alpha}{2c_s^2}\right)\right] \quad (3)$$

$$f_i^{eq}(\mathbf{x}, t) = w_i\phi\left[1 + c_s^2\rho\left(\frac{e_{i\alpha}\,u_\alpha}{c_s^2} + \frac{e_{i\alpha}\,u_\alpha e_{i\beta}\,u_\beta}{2c_s^4} - \frac{u_\alpha u_\alpha}{2c_s^2}\right)\right] \quad (4)$$

where p is the hydrodynamic pressure, ρ is the density and ϕ is the function of the index.

The macroscopic variables are given by He et al. (1999) [24], as follows.

$$\phi = \sum f_i \quad (5)$$

$$p = \sum g_i + \frac{\Delta t}{2}u_\beta\left(-\frac{\partial\psi(\rho)}{\partial\beta}\right) \quad (6)$$

where ψ is a function of ρ and ϕ, whereas:

$$\psi(\rho) = p - c_s^2\rho \quad (7)$$

$$\psi(\phi) = p_{th} - c_s^2\phi \quad (8)$$

here pth is the thermodynamic pressure. It can be calculated from the Carnahan–Starling EOS, and defined as follows:

$$p = \rho RT\frac{1 + \frac{b\rho}{4} + \left(\frac{b\rho}{4}\right)^2 - \left(\frac{b\rho}{4}\right)^3}{\left(1 - \frac{b\rho}{4}\right)^3} - a\rho^2 \quad (9)$$

The challenge during the implementation of Eq. (9) is to find the two-phase equilibrium system under the assumption of a constant temperature. It requires a Maxwell construction as shown in Fig. 1. It specifies the equilibrium states under the assumption of the temperature is achieved if the area of A1 is equal to the area of A2. Here the Maxwell construction is also known as "the equal-area rule". The next task is to find the pressure point, whereas the A1 is equal to the A2. Here an iterative approach is required. Furthermore, a simple procedure can be explained as follows. Specify the system temperature at a sub-critical or below the critical temperature firstly. Here it is postulated that the lower the specified temperature, the wider the coexistence of both low and high-density fluids. At the specified temperature, the Carnahan–Starling EOS is plotted.

The shape of the plot has three intersections points with the horizontal line of the equilibrium pressure line as shown clearly in Fig. 1. A careful estimation of the pressure line should be made, because a wrong estimation cannot estimate the crossing three points *Vm1*, *Vm2*, and *Vm3*. The *Vm1* and *Vm2* are the integral borders to calculate the area *A1* numerically, and *Vm2* and *Vm3* are used to calculate area *A2*. If *A1* is greater than *A2*, the pressure line shifts down and the new three points *Vm1*, *Vm2* and *Vm3* can be found. If *A1* is lower than *A2*, the pressure line shifts up and the *Vm1*, *Vm2* and *Vm3* can be calculated. With the new three points, the above integral calculation runs until the conditions of $A1 = A2$ is accepted in a certain numerical criterion.

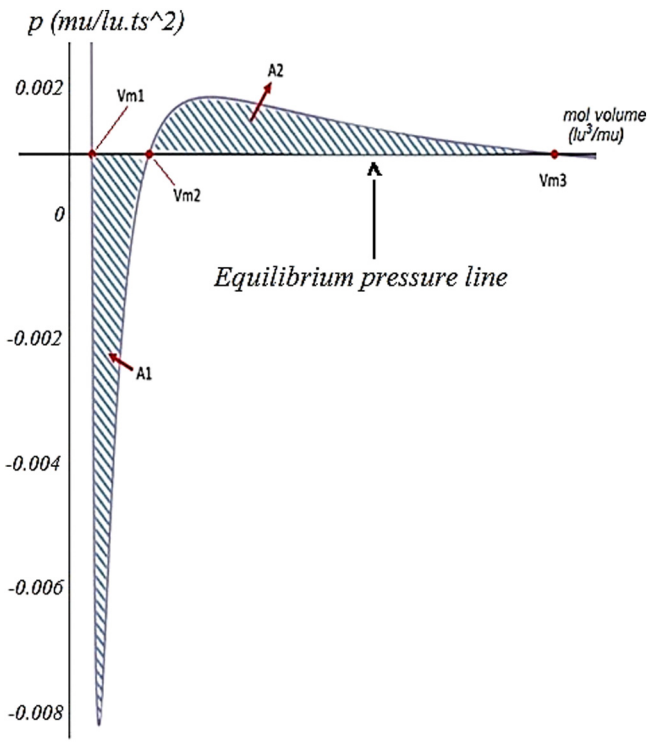

Fig. 1. Maxwell construction for the Carnahan–Starling EOS.

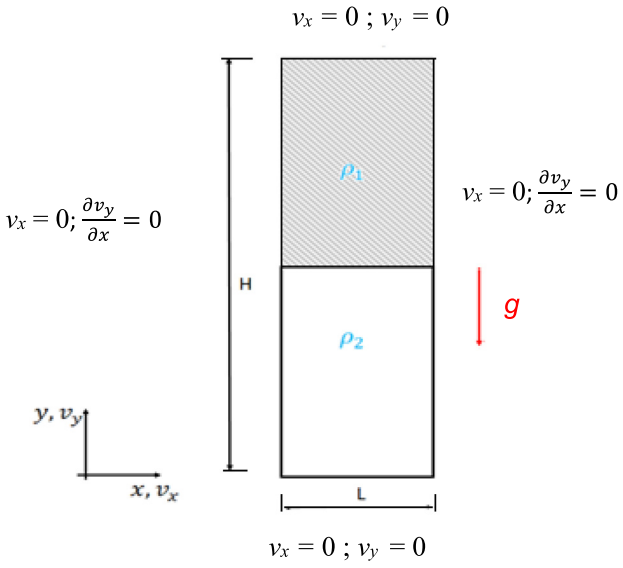

Fig. 2. Schematic diagram of the numerical model.

2.1. Numerical modeling

In the present work, the calculation model for the test case is shown in Fig. 2. As shown in the figure, the aspect ratio of the domain is 1:4. The initial condition of the perturbation is defined as $y = 0.5H + 0.1cos(n)$. Here H is the height of domain, n is the wave-number, and x is the horizontal lattice.

In the present model, the bounce-back boundary conditions are applied at both the top and bottom, while the periodic boundary conditions are applied at both the left and right sides. Here, it is assumed that there is no fluid flow in both x and y-directions. In the calculations, two dimensionless parameters were used. Those are Atwood and Reynolds numbers, posed also in lattice unit (*lu*) for length, mass unit (*mu*) for mass and time step (*ts*) for time. The Reynolds number is defined as:

$$Re = \frac{L}{v}\sqrt{L \cdot g} \quad (10)$$

where L is the size of bottom length, g is the gravity acceleration and v is the dynamic viscosity. The Atwood number is defined as:

$$A_t = \frac{\rho_1 - \rho_2}{\rho_1 + \rho_2} \quad (11)$$

where ρ_1 is the heavy fluid density and ρ_2 is the light fluid density. The time-domain (T) is normalized by the characteristic time of $\sqrt{\frac{L}{g}}$.

2.2. Numerical solution

The basic property LBM is the discrete-velocity distribution function of $f_i(\boldsymbol{x}, t)$, whereas the physical interpretation is the

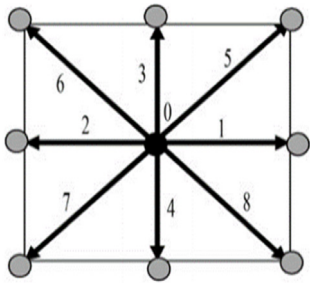

Fig. 3. Schematic diagram of D2Q9.

Table 1
Values of w_i and c_i for D2Q9 scheme.

f_i	0	1	2	3	4	5	6	7	8
w_i	$\frac{4}{9}$	$\frac{1}{9}$	$\frac{1}{9}$	$\frac{1}{9}$	$\frac{1}{9}$	$\frac{1}{36}$	$\frac{1}{36}$	$\frac{1}{36}$	$\frac{1}{36}$
c_{ix}	0	1	−1	0	0	1	−1	−1	1
c_{iy}	0	0	0	1	−1	1	1	−1	−1

particle population. The particle population has a specific velocity $\boldsymbol{c}_i$ at position $\boldsymbol{x}$ and at time t. The mass density and the momentum are calculated through the weighted sums of $\rho(\boldsymbol{x}, t) = \sum_i f_i(\boldsymbol{x}, t)$ and $\rho\boldsymbol{u}(\boldsymbol{x}, t) = \sum_i \boldsymbol{c}_i f_i(\boldsymbol{x}, t)$, respectively. The movement of the particles in LBM must be defined at the beginning as DmQn scheme. The value of m equal to 2 means two-dimensional (2-D) simulation and m equal to 3 means three-dimensional (3-D) simulation. The value of n shows the probabilities of the particle velocity path after the collisions. Typical popular schemes are D2Q9 for 2-D and D3Q19 for 3-D simulation. In D2Q9 means that the simulation is carried-out in 2D and 9 velocity path after each collision. Meanwhile, D3Q19 means that the simulation is carried-out in 3-D and has 19 velocity paths after the collision.

The solution in LBM is comprised in two steps. Those are the collisions and the streaming. The discretized equation of the collision part is defined as:

$$f_i^*(x, t) = f_i(x, t) - \frac{\Delta t}{\tau}(f_i(x, t) - f_i^{eq}(x, t)) \tag{12}$$

Moreover, the discretized equation of the streaming part is defined as:

$$f_i(x + c_i\Delta t, t + \Delta t) = f_i^*(x, t) \tag{13}$$

The collected-particles movement in LBM follows a certain scheme. In the present work, the D2Q9 scheme was used, in which there are two-dimensional space and nine possibilities of the movements after the collision, as shown clearly in Fig. 3. The scheme of D2Q9 has the probability factor in each direction (w_i) known as *the weight factor* and *speed direction* of c_i. The values of w_i and c_i in the D2Q9 scheme are shown in Table 1.

Furthermore, the discrete equations of f_i and g_i are given as follows:

$$f_i(x + \boldsymbol{e_i}\delta_t, t + \delta_t) - f_i(x, t) = -\frac{\delta_t(f_i(x, t) - f_i^{eq}(x, t))}{\tau_f} - \frac{2\tau_f - 1}{2\tau_f}\frac{(\boldsymbol{e_i} - u).\nabla\psi(\phi)}{RT}\Gamma_i(u)\delta_t \tag{14}$$

$$g_i(x + e_i\delta_t, t + \delta_t) - g_i(x, t) = -\frac{\delta_t(g_i(x, t) - g_i^{eq}(x, t))}{\tau_g} - \frac{2\tau_g - 1}{2\tau_g} \times (e_i - u).[\Gamma_i(\boldsymbol{u}).(F_s + G) - (\Gamma_i(u) - \Gamma_i(0))\nabla\psi(\rho)]\delta_t \tag{15}$$

whereas,

$$\Gamma_i(u) = w_i[1 + \frac{\boldsymbol{e_i}.\boldsymbol{u}}{RT} + \frac{(\boldsymbol{e_i}.\boldsymbol{u})^2}{2(RT)^2} - \frac{\boldsymbol{u}^2}{2RT}] \tag{16}$$

$$f_i^{eq} = w_i\phi[1 + \frac{\boldsymbol{e_i}.\boldsymbol{u}}{RT} + \frac{(\boldsymbol{e_i}.\boldsymbol{u})^2}{2(RT)^2} - \frac{\boldsymbol{u}^2}{2RT}] \tag{17}$$

$$g_i^{eq} = w_i[p + \rho RT(\frac{\boldsymbol{e_i}.\boldsymbol{u}}{RT} + \frac{(\boldsymbol{e_i}.\boldsymbol{u})^2}{2(RT)^2} - \frac{\boldsymbol{u}^2}{2RT})] \tag{18}$$

The values of τ_f and τ_g are the relaxation times relating to the kinematic viscosity and the mobility, respectively. The index function (ϕ), the pressure (p), the macroscopic velocity ($\boldsymbol{u}$), the density (ρ), the kinematic viscosity (υ), and the force on the surface (F_s) are defined respectively as follows:

$$\phi = \sum \overline{f_i} \tag{19}$$

$$p = \sum \overline{g_i} - \frac{\boldsymbol{u}}{2}.\nabla(p - \rho RT)\delta_t \tag{20}$$

$$\rho RT\boldsymbol{u} = \sum \boldsymbol{e_i}\overline{g_i} + \frac{RT}{2}(F_s + G)\delta_t \tag{21}$$

$$\rho(\phi) = \rho_l + \frac{\phi - \phi_l}{\phi_h - \phi_l}(\rho_h - \rho_l) \tag{22}$$

$$\upsilon(\phi) = \upsilon_l + \frac{\phi - \phi_l}{\phi_h - \phi_l}(\upsilon_h - \upsilon_l) \tag{23}$$

$$F_s = \kappa\rho\nabla\nabla^2\rho \tag{24}$$

The ψ is the variable function to represent the intermolecular interaction in the multiphase system. It has a relationship with the non-ideal EOS of a density function (ρ) and index function (ϕ), and is defined as follow.

$$\psi(\rho) = p - {c_s}^2\rho \tag{25}$$

$$\psi(\phi) = p_{th} - {c_s}^2\phi \tag{26}$$

The Cahn–Hilliard-like equations for the interface tracking were derived as follows (Huang, 2015) [18]. The Taylor expansion of Eq. (2) and applying the Chapman–Enskog expansion to $\partial_t = \partial_{t1} + \varepsilon\,\partial_{t2}$ and fi $= f_i^{(0)} + \varepsilon f_i^{(1)} + \varepsilon^2 f_i^{(2)}$, where $\varepsilon = \Delta t$, we will get as follows

$$\varepsilon(\partial_{t1} + \varepsilon\,\partial_{t2} + e_{i\alpha}\,\partial_\alpha)[f_i^{(0)} + \varepsilon f_i^{(1)} + \varepsilon^2 f_i^{(2)}] + 0.5\varepsilon^2(\partial_{t1} + \varepsilon\partial_{t2} + e_{i\alpha}\,\partial_\alpha)^2[f_i^{(0)} + \varepsilon f_i^{(1)}] = -\frac{1}{\tau_1}[f_i^{(0)} + \varepsilon f_i^{(1)} + \varepsilon^2 f_i^{(2)} - f_i^{(eq)}] + S_i\Delta t \tag{27}$$

Maintaining the terms to O(ε^2) of above equation yields,

$$O(\varepsilon^0): \frac{1}{\tau_1}[f_i^{(0)} - f_i^{(eq)}] = 0, \tag{28}$$

$$O(\varepsilon^1): (\partial_{t1} + e_{i\alpha}\partial_\alpha)f_i^{(0)} + \frac{1}{\tau_1}f_i^{(1)} - S_i = 0, \tag{29}$$

$$O(\varepsilon^2): \partial_{t2}f_i^{(0)} + (1 - \frac{1}{2\tau_1})(\partial_{t1} + e_{i\alpha}\partial_\alpha)f_i^{(1)} + 0.5(\partial_{t1} + e_{i\alpha}\partial_\alpha)S_i + \frac{1}{\tau_1}f_i^{(2)} = 0 \tag{30}$$

From Eqs. (5) and (28) we get $\sum f_i^{(0)} = \phi$ and $\sum f_i^{(n)} = 0$, for n $\geq$ 1. Summing both sides of Eq. (29) over i yields

$$\partial_{t1}\phi + \partial_\alpha(\phi u_\alpha) = 0 \tag{31}$$

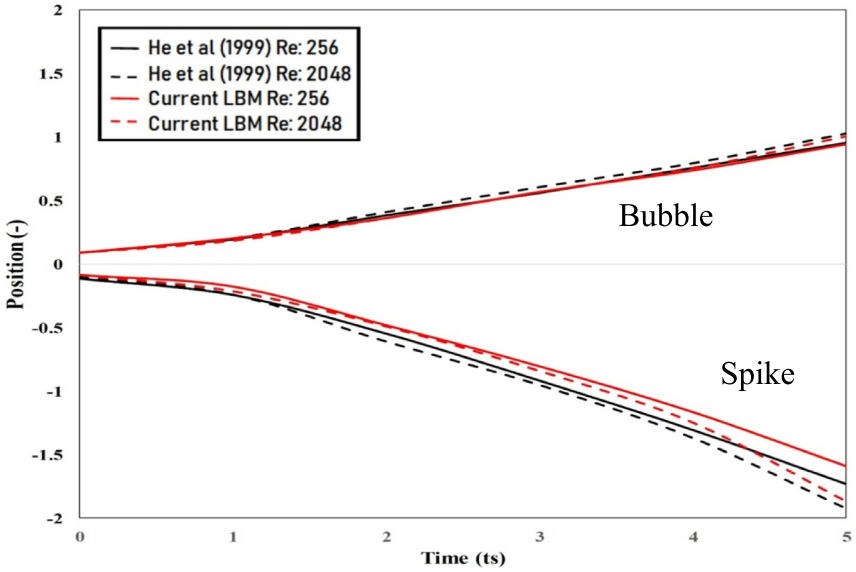

Fig. 4. The comparison between the observed bubbles and spikes positions obtained from the present work and He et al. (1999) [24].

Summing Eq. (30) over i yields

$$\partial_{t2}\phi + (1 - \frac{1}{2\tau_1})\partial_\alpha[\sum e_{i\alpha} f_i^{(1)}] + 0.5\ \partial_\alpha[\sum e_{i\alpha} S_i'] = 0 \tag{32}$$

The term of $\sum e_{i\alpha} f_i^{(1)}$in simulation were omitted and substitute the $\sum e_{i\alpha}\ S_i' = (1 - \frac{1}{2\tau_1}) F_\alpha'$ into Eq. (32), we get

$$\partial_{t2}\phi + 0.5(1 - \frac{1}{2\tau_1})\partial_\alpha\ F_\alpha' = 0 \tag{33}$$

Replacing $F_\alpha' = -\partial_\alpha(p - c_s^2\phi)$ into the Eq. (33) will result

$$\partial_{t2}\phi - 0.5(1 - \frac{1}{2\tau_1})\partial_\alpha[\partial_\alpha(p - c_s^2\phi)] = 0 \tag{34}$$

Combination of Eqs. (31) and (34) results

$$\partial_{t1}\phi_+ \partial_\alpha(\phi u_\alpha) = 0.5(1 - \frac{1}{2\tau_1})\partial_\alpha[\partial_\alpha(p - c_s^2\phi)] \tag{35}$$

The Eq. (35) is the macroscopic interface-tracking equation. It is known also the Cahn–Hilliard-like equation.

3. Validations

The first validation was carried out by the comparison of the obtained results from the present work with that of He, et al. (1999) [24] as shown in Fig. 4. The flow condition was At = 0.5 and Re = 256 and 2048 [24]. The figure shows that the bubbles and spikes positions obtained from present work are identical to that of He, et al. Next, the spike positions have a small discrepancy, and those are 5.7% (in the case Re = 2048) and 12.6% (in the case Re = 256). The spike distance under the same Atwood number of 0.5 means the same gravity force. Next, the difference of spike-traveled gap between the Re = 256 (12% spike gap) and Re = 2048 (5.7% spike gap) is from the effect of the viscosity. Under the condition of Re = 256 it is considered that it has a higher viscosity than that of Re = 2048. This means that the increase of viscosity will increase the friction force. Moreover, these facts indicate that the obtained results from the present numerical simulation are in a good agreement with those of He et al.

The next validations were conducted by using the comparison of the results from the present works with those of Lee, et al. Ding, et al. Guermond et al. and Tryggvason. Here Lee et al. [32] conducted the numerical simulation by using the Navier–Stokes Cahn–Hilliard based with a finite difference method. Ding et al. [33] obtained the simulation result using the Navier–Stokes with a phase-field method. Guermond et al. [34] carried-out the simulation by using the Navier–Stokes finite element method, meanwhile Triggvasson used the Navier–Stokes based with a vortex in the cell in his work [35]. The results are shown in Fig. 5. Close observation of Fig. 5 indicates that the current work conforms well with the above previous works. The bubbles and spikes positions deviate around only 2% and 7%. Those agreements show the capability of the current numerical scheme in comparison with the other methods to simulate the RTI.

The validation was also performed also by the comparison of present numerical work with the experimental results from Waddell et al. (2001) [26]. In their experiment, the salt solution and surfactant-additive-heptane were used as the tested fluids. The Atwood numbers were 0.155 and 0.336 [26]. The result is shown in Fig. 6. The figure indicates that both experimental and simulation results are also in a good agreement. The figure depicts that the amplitude due to gravity and buoyancy forces increases with the time after sled release. Here the gravity pulls the high density fluid to descend; meanwhile the buoyancy force pushes the low density fluid to fill the area that was leaved by the high density fluid. Next, the linear growth happens in the range of time below 0.1 s or until the amplitude of 4 mm as shown clearly in Fig. 6.

The non-linear growth area when the time after sled greater than 0.1 s is also shown in Fig. 6. The non-linear growth area shows that the amplitude of both experimental and numerical always less than the amplitude of theoretical results. This difference due to the complicated interfacial structure on the experimental that makes the prevailed-force becomes more complex. Meanwhile, the theoretical model only counts the ideal mathematical conditions.

4. Results and discussions

In the LBM simulation, the values of high and low densities must be set as the calculation inputs. The combinations of both densities are represented by Atwood number. In the present simulation, under a constant Reynolds number of 1024, the Atwood numbers ranged from 0.1–0.5. Next, the Reynolds numbers were varied at 256, 512, 1024 and 2048, whereas the Atwood number

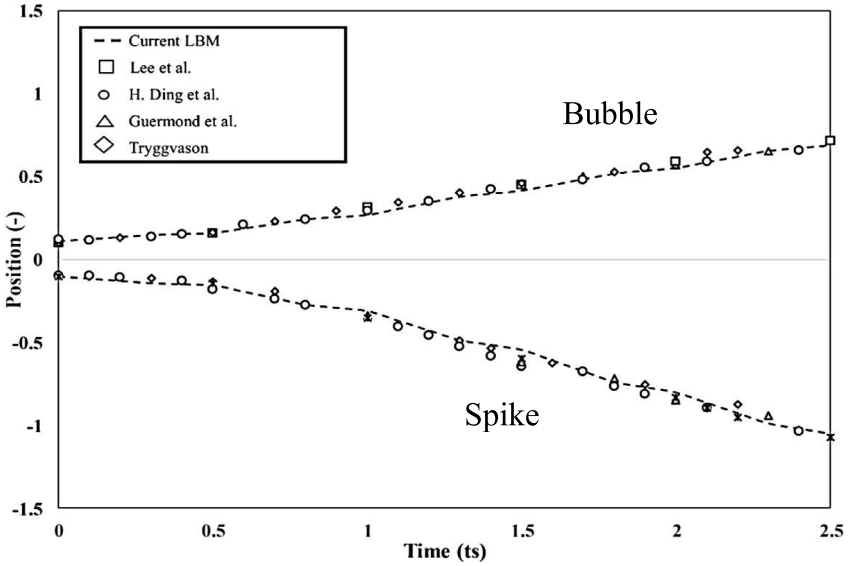

Fig. 5. The comparison of present work with those of Lee, et al. H Ding, et al. Guermond et al. and Tryggvason [32–35].

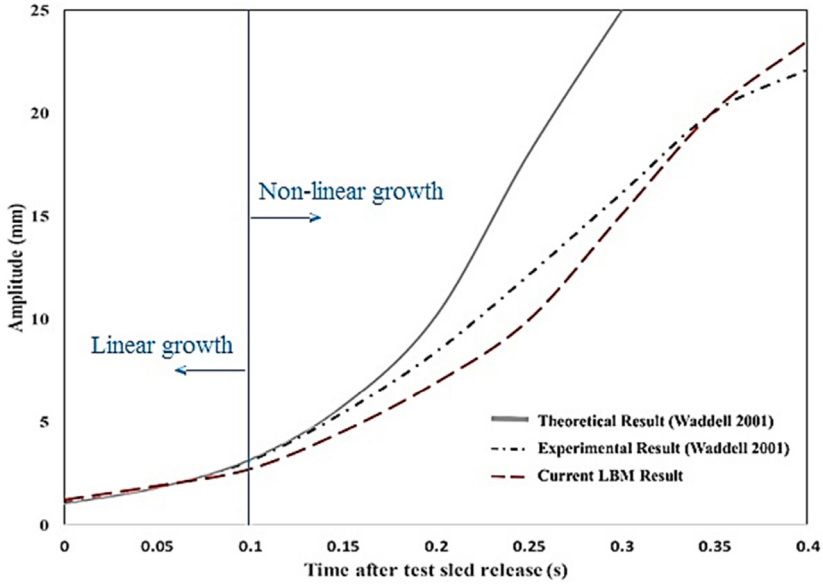

Fig. 6. The comparison between the present numerical result with the experimental result from Waddell (2001) [26].

was kept constant at 0.5. The calculation results of both densities are shown in Table 2.

Table 2 shows the obtained characteristics of Maxwell construction by using Carnahan–Starling EOS. The table reveals that the decrease of the critical temperature will increase and decrease the high mole volume (V_{m3}) and low mole volume (V_{m1}) respectively. Consequently, it increases both the ratio density and Atwood number.

Fig. 7 shows the time progress of the development stage of the interfacial behavior obtained from the present work. The figures show that the interfacial behavior during RTI can be described into four-shape stages. Those are (1) Perturbation continuation, (2) head-and-neck shape, (3) Kelvin–Helmholtz Instability (KHI) or mushroom shape, and (4) turbulence flow. The perturbation continuation stage (Fig. 7(a)) occurs when the interface has a sinusoidal-like-shape and will end when the spike is in the form of the head-and-neck development (Fig. 7(b)). The head–neck stage is started when the spike-width is bigger than the stem. The KHI begins when the spike-edge at the right and left sides form the rolls-up. As time goes by, the rolls-up of the both-side form a mushroom-shaped (Fig. 7(c)). The turbulence stage is begun when both the right and left sides of the spikes are pulled up in the bubble ascending direction (Fig. 7(d)).

RTI occurs only when the spikes accelerate in the direction of lighter density. Here, the bubble and spike movements have different mechanism. The spikes descend because of the gravity force. Otherwise, the bubbles ascend only as the impulsive reason to fill the room that was left by higher density fluid. The initial condition of a sinusoidal expedites the movement both of bubble and spike. The lower part of the interface as the onset of spike has less supported-pressure than that is required to stand still. The condition makes the spike initiates to go-down. The highest portion of the bubble has a higher pressure than the other portion. The bubble begins to ascend and push aside the higher density fluid. In the next section, the movement process of the bubble and spike will be discussed.

Table 2
The calculation result of Maxwell construction of Carnahan–Starling EOS.

The factor of critical temperature (T/T_C)	Equilibrium pressure	High mole volume (V_3)	Low mole volume (V_1)	High density ($\rho_h = 1/V_1$)	Low density ($\rho_l = 1/V_3$)	Atwood number
9.99E−1	4.38E−3	8.50	6.96	1.44E−1	11.76E−2	0.1
9.94E−1	4.28E−3	9.51	6.34	1.58E−1	10.52E−2	0.2
9.85E−1	4.09E−3	10.76	5.79	1.73E−1	9.30E−2	0.3
9.72E−1	3.83E−3	12.34	5.28	1.89E−1	8.11E−2	0.4
9.54E−1	3.50E−3	14.52	4.84	2.07E−1	6.89E−2	0.5

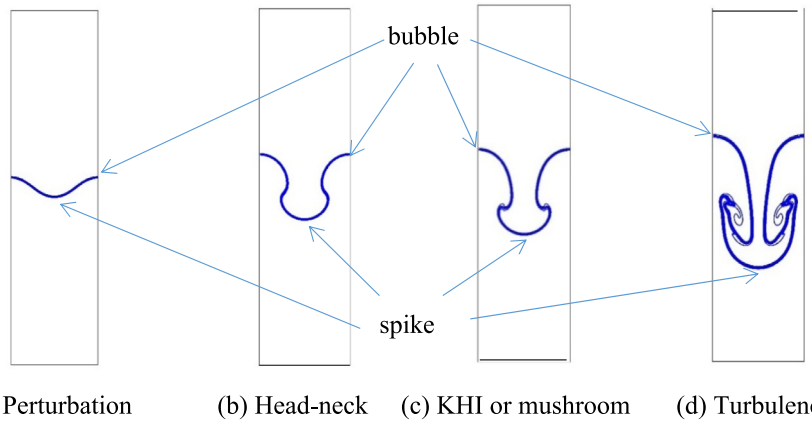

Fig. 7. RTI interface shape stages.

Table 3
The summary of the interfacial stage under various Reynolds numbers.

Time step	Reynolds number			
	256	512	1024	2048
1	P	P	P	P
2	P	H	H	H
3	H	K	K	K
4	T	T	T	T
5	T	T	T	T

Note: P = perturbation, H = Head-and-neck, K = Kelvin–Helmholtz instability, T = Turbulence.

Table 4
The summary of the interfacial stages under various Atwood numbers.

Time step	Atwood number				
	0.1	0.2	0.3	0.4	0.5
1	P	P	P	P	P
2	P	P	H	K	K
3	P	H	K	K	K
4	P	H	T	T	T
5	H	K	T	T	T

Note: P = perturbation, H = Head-and-neck, K = Kelvin–Helmholtz instability, T = Turbulence.

Fig. 8 shows the effect of the Reynolds number on the time variation of the interfacial behavior during RTI, whereas the summary of the interfacial stages is tabulated in Table 3. From Fig. 8(a) and Table 3, it is noticed that at T = 1 under all Reynolds numbers, it poses a perturbation stage. Here at T = 1 is marked as the early stage when the heavy fluid starts to descend and the light fluid begins to ascend. The similarity of the interface shape at this early stage means that the liquid viscosity has no significant effect on the initiation of the RTI. From Fig. 8(b) and Table 3, at T = 2 the effect of Reynolds number on the interfacial from a perturbation stage to the head–neck stage can be shown. Close investigation of Fig. 8(a) and (b) reveals that at T = 1 and T = 2, the interface is insensitive to the change of the Reynolds number. The insensitiveness is shown by the overlapped-interfacial under the change of the Reynolds numbers. Meanwhile, the Reynolds number plays an important role at T = 3 – 5 as shown in Fig. 8(c) – (e). Here it is noticed that the higher Reynolds number, the more developed the RTI stages.

The physical description of the obtained results can be explained that the interfacial movement occurs due to the interaction of the gravity and the friction forces. The gravity force pulls down the heavier fluid and, consequently, pushes up the lighter fluid. Both the internal and interfacial frictions forces dampen the movement. The internal-friction-damping force is resulted from the both working fluid viscosities. Meanwhile, the interfacial friction is caused by the immiscible behavior of both working fluids. The increase of the Reynolds number means the decrease of the viscosities effect, therefore the internal friction forces play a less important role than the gravity force.

Fig. 9 shows the effect of Atwood number on the time variation of the interfacial behavior during RTI. Moreover, the summary of the interfacial stages is shown in Table 4. The main difference between Figs. 8 and 9 is that the interfacial behavior is more sensitive under the change of the Atwood number. The sensitivity becomes stronger as the time progress. The strong sensitivity can be seen from the separated-interfacial under various Atwood numbers since T = 1. The physical explanations of Atwood number effects on the interfacial behavior during RTI can be described as follows. The higher the Atwood number, the higher the difference of densities between both involved-fluids, consequently the higher the influence of gravity-force and the more velocity mixing during RTI.

The complicated structure of interface shape during RTI needs more quantitative explanations. Here, the average density profile is used to quantify the characteristics of the horizontal mixing layer as conducted also by [22,24]. The quantity of the horizontal lattice or the average density layer shows the mixture behavior at the specific time steps. Here, the average density (ρ_{ave}) is calculated by averaging the density along the horizontal cross-section, and defined as follows

$$\rho_{ave} = \frac{\sum_i^n \rho_i}{n} \tag{36}$$

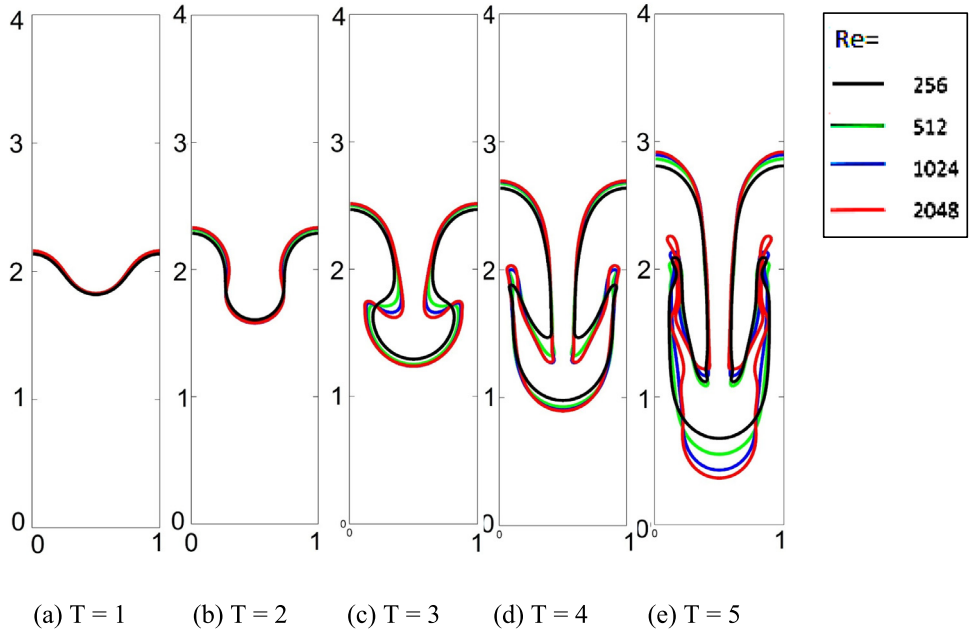

Fig. 8. The effect of Reynolds number on the time variation of interfacial behavior during RTI.

where, $\sum_i^n \rho_i$ is the total density along the horizontal cross-section and n is the total number of the horizontal lattice. In the present numerical work, the effects of both Reynolds and Atwood numbers on the average density are considered. Fig. 10 presents the comparison of average density plots at T = 1. In the figure, (a) and (b) correspond to the effect of Reynolds number and Atwood number, respectively. Close observation of Fig. 10(a) reveals that under the change of the Reynolds number, the shape of average density poses a similar shape. The similarity of average density is in accordance with the similarity of the corresponding interfacial plot as shown in the lower part of Fig. 10. The average density means the mixture situation in horizontal physically. Hence, this similarity is supported with the similarity in interfacial shape. In addition, the zoomed plot in the box of Fig. 10(a) relates to the RTI development and represents the interfacial position of the bubbles. The figure also depicts that the increase of the Reynolds number will shift the bubbles into the faster-ascending movement.

Fig. 10(a) also shows that the spikes interfacial average densities do not significantly change with the Reynolds number. It marked as overlapped average density plot in the figure. This fact means that at the early stage, the effect of the Reynolds number on the bubbles movement is more dominant than that of the spikes. Moreover, the effect of Atwood number on the interfacial shape at T = 1 is shown in Fig. 10(b). The main difference between Fig. 10(a) and (b) is the occurrence of non-overlap of the average density profile due to the change of the Atwood number. This means that the Atwood number affects the interfacial behavior since the beginning of RTI.

The rigorous-asymptotic analysis was investigated and compared to the heuristic model for this perturbation staged by Danilov [23]. The results of the fingering structure and mushy region for the density averaging are very similar to the present perturbation stage obtained from the present work (Fig. 10). Briefly, Danilov proposed as follows. The stratified interface fluids function addressed as $\Gamma_t = y = \varphi(x/\varepsilon, x, t)$ in dimensionless variables. The function $\varphi(\xi, x, t)$ is periodic in ξ, so $\varphi(\xi + 1, x, t) = \varphi(\xi, x, t)$ and this is fingering structure function. The averaging equation through the asymptotic solution was found $\frac{\partial \overline{\rho}}{\partial t} + [\nabla, \bar{\bar{u}}\,\overline{\rho}] + F(\overline{\rho}) = 0$. While, the averaging through heuristic model was found $\frac{\partial \rho}{\partial t} + [v, \nabla\rho\,] + \frac{\partial F(\rho)}{\partial y} = 0$. This result encourages the next analytic model in order to investigate the subsequent stage such as head–neck, KHI and turbulence.

Fig. 11 presents the effect of both Reynolds and Atwood numbers on the average density at T = 2. The figures show that the Atwood number poses a more dispersed-plot than that of the Reynolds number. Close observation of the effect of the Reynolds numbers effect as shown in Fig. 11(a) reveals that under the investigated range of Re = 256 until 2048, they pose only the perturbation stage and the head–neck stage. This means that by eight times multiplication of the Reynolds number makes differences in RTI mixing stages from perturbation to head–neck. On the other hand, the effect of the Atwood numbers as shown in Fig. 11(b), reveals that under the investigated range of At = 0.1 until 0.5, they pose three-stages: perturbation, head–neck and KHI. This means that by five-times multiplication of the Atwood numbers produces more advances in the RTI process.

The effects of both Reynolds and the Atwood numbers on the average density at T = 3 are presented in Fig. 12, in which Fig. 12(a) shows the general shape of the peak and valley of the average density due to the change of the Reynolds numbers. The corresponding interfacial shape on the lower part also shows the head–neck and KHI stages. On the other hand, the effect of Atwood number on the corresponding average density is depicted in Fig. 12(b). The main difference between Fig. 12(a) and (b) is the occurrence of the small peak on the valley during the KHI when the Atwood number is changed. The small peak in Fig. 12(b) corresponds to the tip of the tail on the interfacial shape; meanwhile it is not existed in Fig. 12(a).

Fig. 13 shows the effect of both Reynolds and Atwood number on the average density at T = 4. The observed phenomena are as follows. In Fig. 13(a) the small peaks on the average density plots are detected. The small tips correspond to the small tip of the tails of KHI on both sides. On the other hand, the appearance of the small peak under the variation of the Atwood number at the previous stage (T = 3) has been continuing into an advance process. It is marked with a stretching area between both the main and the small peaks as shown in Fig. 13(b). Here, the stretched-area corresponds to the turbulence flow stage.

Furthermore, the effects of both Reynolds and Atwood number on the average density at T = 5 are shown in Fig. 14. Closed

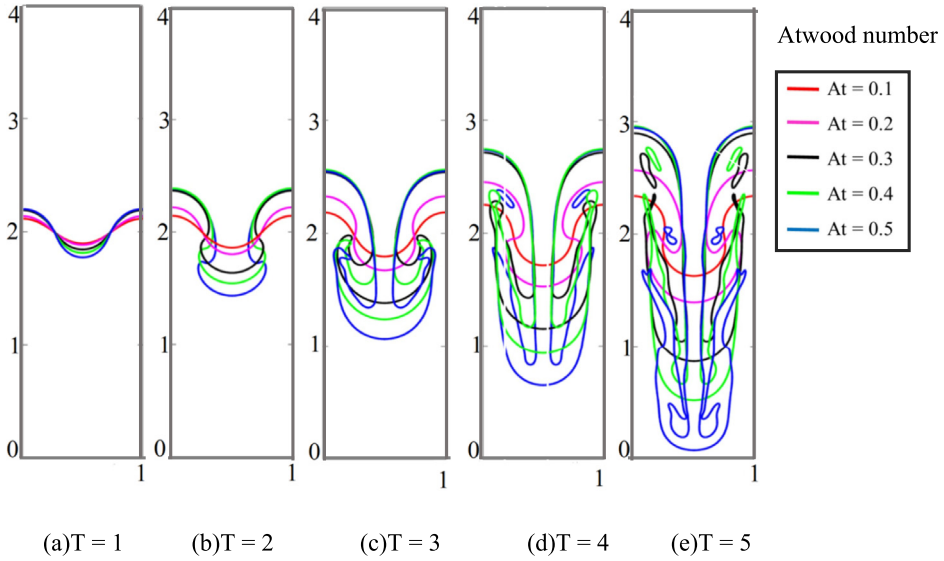

Fig. 9. The effect of the Atwood number on the time variation of the interfacial behavior during RTI.

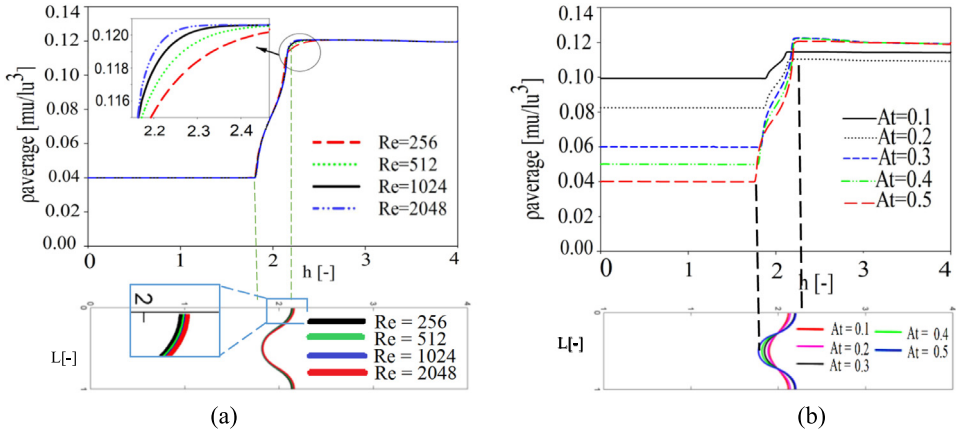

Fig. 10. The effect of (a) the Reynolds number and (b) the Atwood number on the average density at T = 1.

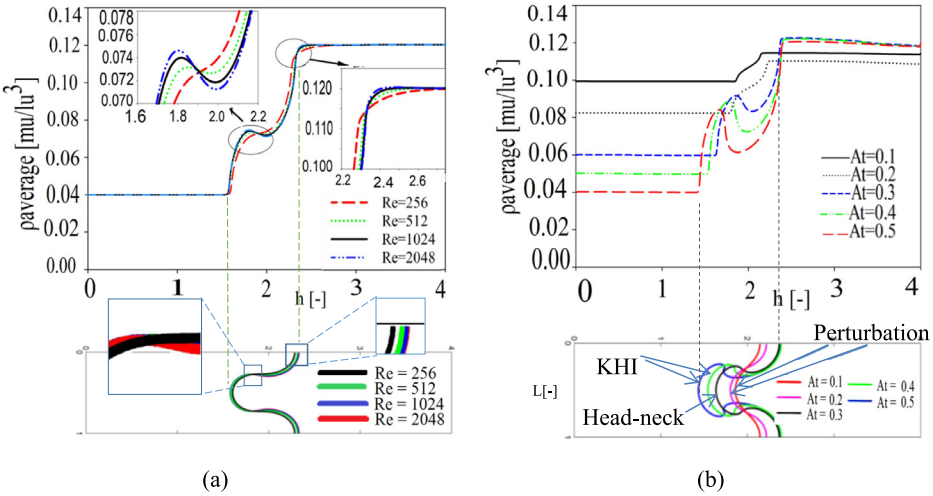

Fig. 11. The effect of (a) the Reynolds number and (b) the Atwood number on the average density at T = 2.

observation of the Figures indicates that under the variation of Reynolds number, the stretched area between both the main and small peaks is found as shown in Fig. 14(a). The stretched area corresponds to the turbulence stage. On the other hand, the increase of the Atwood numbers to T = 5 produces a higher oscillation of average density, as shown in Fig. 14(b). The stretched

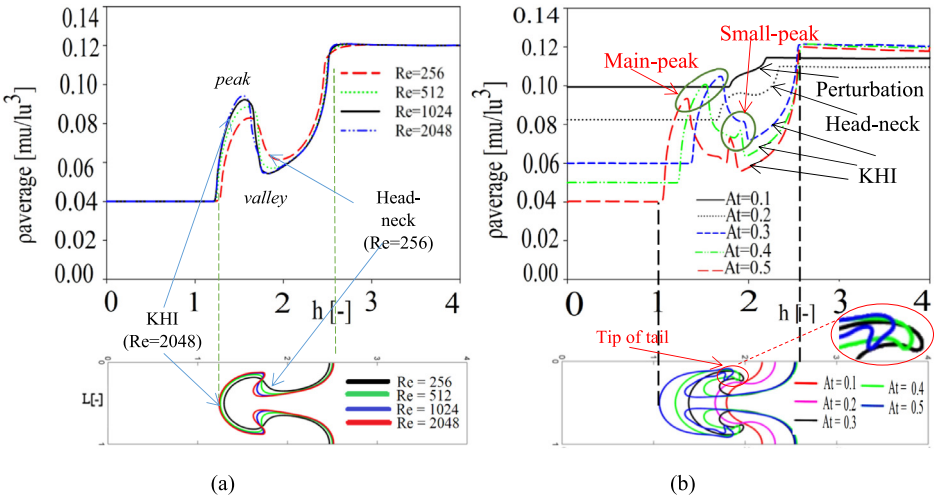

Fig. 12. The effect of (a) the Reynolds number and (b) the Atwood number on the average density at T = 3.

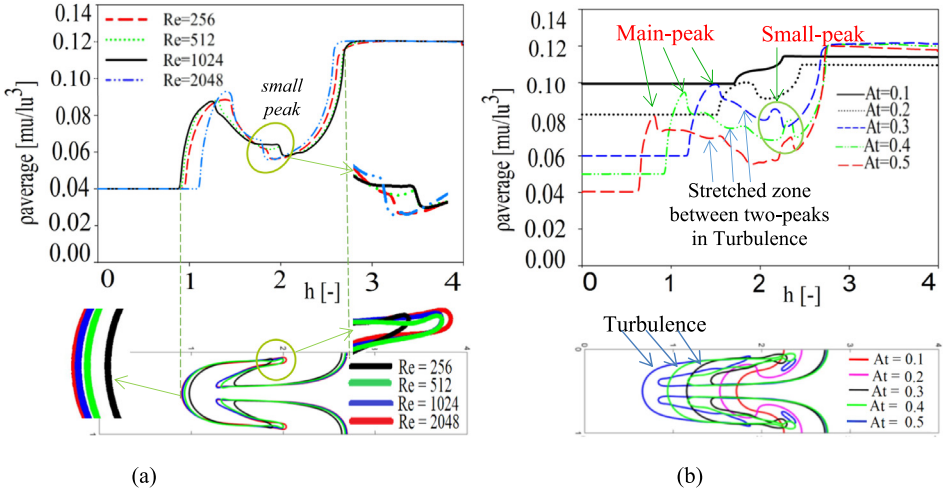

Fig. 13. The effect of (a) Reynolds number and (b) Atwood number on the average density at T = 4.

area at the previous step (T = 4) turns into a random wave at T = 5. The other obtained characteristics of average density profile are the appearances of the valley due to the bubbles trapped and the peaks due to the tails detachment as shown in Fig. 14(b). In addition, the comparison of the effects between Atwood and Reynolds numbers indicates that the Atwood number is more dominant than the Reynolds number. The physical explanation of the obtained phenomenon is that the gravity force dominates over the viscosity friction. This fact can be seen that in RTI flows, the gravity force takes part as the primary mover and the viscosity friction force is the reaction to the primary force.

In the next section, a quantitative analysis of two-fluid interface during the RTI process in vertical orientation will be discussed in the form of the positions of the bubble and the spike. The effects of Reynolds number on the positions of both the bubbles and spikes are shown in Fig. 15. Here, the difference of the traveled-distance of bubbles and spikes under the flow condition of Re = 256 and Re = 2048 were compared at each time step. For the comparison purposes, the difference of traveled distance (gap) is presented in the form of percentage gap. The percentage gap was determined by the ratio between the gap of the bubbles (spikes) under Re = 256 and 2048 divided by the traveled distance of bubbles (spikes) under Re = 2048. The results are tabulated in Table 5. In the table, two important points should

Table 5
The ratio of traveled-distance of bubbles and spikes distance under Re = 256 and 2048.

Bubble or spike	Time-step				
	T = 1	T = 2	T = 3	T = 4	T = 5
Bubble	1.13%	1.91%	1.97%	2.1%	3.92%.
Spike	0.5%	1.45%	4.16%	8.3%	20.8%

be highlighted as follows. The traveled-gaps of the bubbles at the initial steps (at T = 1 and T = 2) are greater than that of the spikes. Next, the growth of the traveled-gap of the spikes is faster than that of the bubbles as shown at T = 3 to T = 5. This means that the increase of the Reynolds number is resulted from the decrease of the viscosity. The decrease of the viscosity will decrease of dampening force, consequently it makes a faster mixing process.

The effect of the Atwood number on the positions of both bubbles and spikes is presented in Fig. 16. In comparison between Figs. 16 and 15, it is clearly noticed that the effect of Atwood number is more dominant than of the Reynolds number. Here we can see that the width of the positions of both the bubbles and spikes under the variation of the Atwood number are wider than that of the Reynolds number. Here, the position of both the bubbles and the spikes were determined by using the same methods

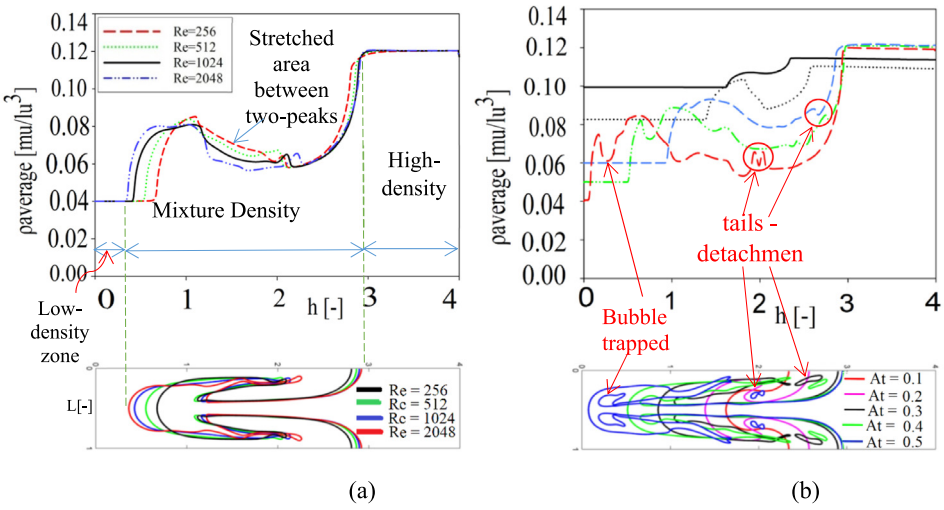

Fig. 14. The effect of (a) Reynolds number and (b) Atwood number on the average density at T = 5.

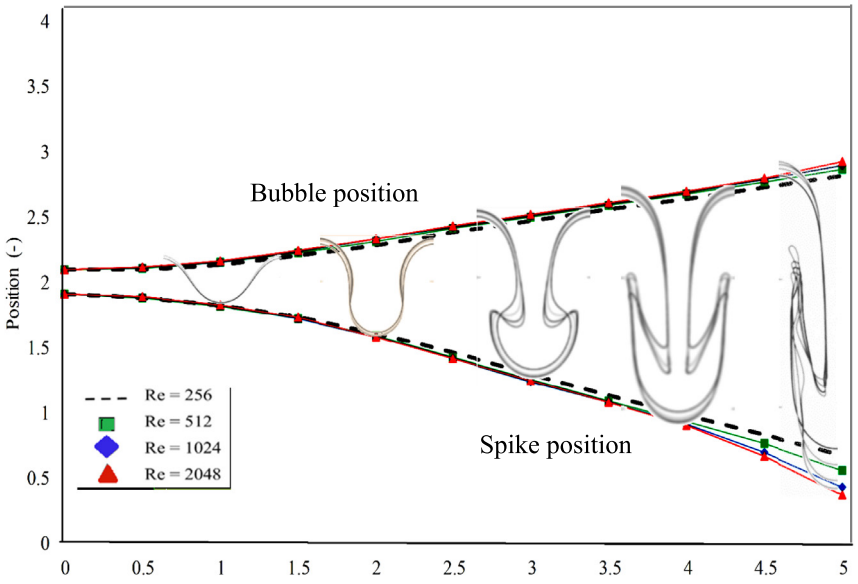

Fig. 15. The effect of the Reynolds number on the position of the bubbles and the spikes.

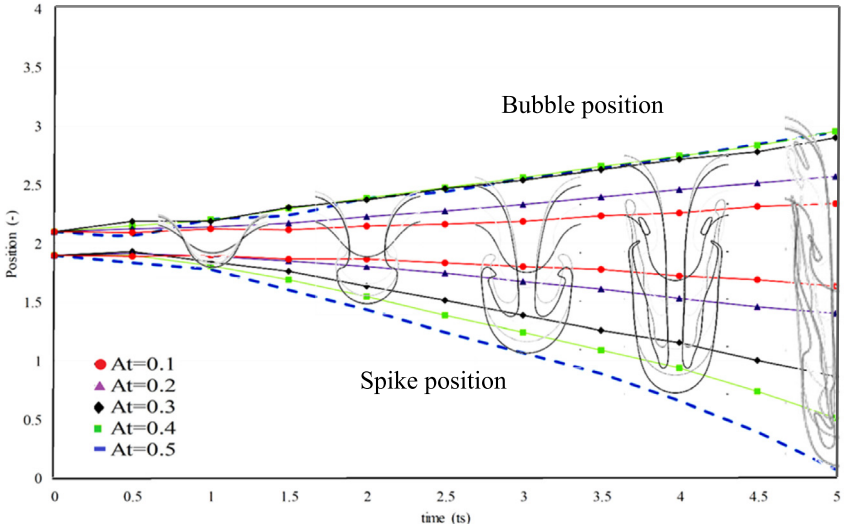

Fig. 16. The effect of the Atwood number on the position of the bubbles and the spikes.

Table 6
The ratio of traveled-distance of bubbles and spikes between At=0.1 and At=0.5.

Bubble or spike	Time-step				
	T = 1	T = 2	T = 3	T = 4	T = 5
Bubble	3.87%	10.92%	16.51%	21.35%	25.78%
Spike	6.58%	23.07%	40.86%	62.04%	95.47%.

as Fig. 15. Here, the percentage of the gap was determined by measure the ratio between the gap of the bubbles or the spikes under the flow condition of At = 0.1 and At = 0.5 divided by the traveled distance of the bubbles or the spikes under the flow condition of At = 0.5. The results are tabulated in Table 6. In comparison between Tables 6 and 5, it is noticed that in Table 6 the gap ratio of spikes from T = 1 to T = 5 are greater than that of the bubbles. Next, the gap ratio of bubbles and spikes under the change of Atwood number is greater than that of bubbles and spikes under the change of Reynolds number. These facts support the indication that the influence of Atwood number is more dominant than that of the Reynolds number.

In the present work, the simulation of two-dimensional (2-D) RTI during the mixing of the immiscible fluids was performed. Zhou et al. (2019) [31] reported that 2-D simulation does not able to capture the important behavior in physics and engineering applications (e.g. inertial confinement fusion (ICF) and supernovae). Here, the turbulence effects in supernovae theory require three-dimensional (3-D) simulation model, whereas they noticed that the drawback of 2-D model in explosion of supernovae tends to exaggerate the axial sloshing. Then the possible misleading to the standing accretion shock instability (SASI) as the aiding factor is appeared. While, the 2-D simulation for ICF construct the axisymmetric flows and has the consequences yields factor of two or more than in experiment or 3D simulation. The perfect momentum balance in 2D simulation maximize the conversion of shell kinetic energy to hotspot internal energy, and hence maximize the compression and heating of the hotspot material, and finally enhance the fusion reactivity. Theoretically, the possibility to extend the 2-D into 3-D configurations is a straight forward in the present LBM method, but need much more computational resources.

In the present LBM, the choice of 2-D and 3-D must be declared from the beginning path probability of particle direction. The scheme of D2Q9 means after once collision in 2D simulation, any particles have 9 probabilities of movement direction. Otherwise, the scheme of typical D3Q19 means that all the particles in 3-D simulation have 19 probabilities of the movement after every single collision. Moreover, 2-D simulation has one lattice of depth, but in 3-D simulation the multiplication computation resources is needed to provide as much as the lattice depth factors. However, in the near future, LBM 3D simulation should be encouraged in order to improve the complex understanding of the RTI.

5. Conclusions

The numerical simulations during the mixing process of RTI have been carried out by using the Lattice Boltzmann method (LBM). Two important parameters of the viscosity and ratio-density of the involved-fluids were considered. The Reynolds number represents the viscosity and the Atwood number represents the ratio density of both working fluids. The analysis of interfacial behavior during RTI, the behavior of the average density, and the positions of bubbles/spikes were presented. The results are summarized as below:

1. Both Reynolds and Atwood numbers affect the RTI process. The higher the Reynolds and the Atwood numbers, the faster the mixing process during RTI.
2. The average density plots show that under the change of the Atwood number is more dispersed than that of the Reynolds number. It indicates that the Atwood number has an important role than the Reynolds number.
3. The distance of traveled (positions at the certain time) of the bubbles and spikes under change of the Atwood number is always higher than that of the change of the Reynolds number. This fact means that change of the Atwood number is more dominant than that of Reynolds number during mixing process of RTI.

Declaration of competing interest

The authors declare that they have no known competing financial interests or personal relationships that could have appeared to influence the work reported in this paper.

Acknowledgment

The present research is a part of Ph.D. works supported by Indonesia Endowment Fund for Education (Lembaga Pengelola Dana Pendidikan/LPDP), Ministry of Finance, Republic of Indonesia.

References

[1] Y. Zhou, Rayleigh–Taylor and Richtmyer–Meshkov instability induced flow, turbulence, and mixing. I, Phys. Rep. 720–722 (2017) 1–136, http://dx.doi.org/10.1016/j.physrep.2017.07.005.
[2] Y. Zhou, Rayleigh – Taylor and Richtmyer – Meshkov instability induced flow, turbulence, and mixing. II, Phys. Rep. 723–725 (2017) 1–160, http://dx.doi.org/10.1016/j.physrep.2017.07.008.
[3] K. Guo, R. Chen, Y. Li, W. Tian, G. Su, S. Qiu, Numerical simulation of Rayleigh–Taylor Instability with periodic boundary condition using MPS method, Prog. Nucl. Energy 109 (28) (2018) 130–144, http://dx.doi.org/10.1016/j.pnucene.2018.08.008.
[4] H. Seo, I.C. Bang, Revisiting the Rayleigh–Taylor instability and critical heat flux with R-123 for different heater sizes and pressures, Int. J. Therm. Sci. 100 (2015) 324–332, http://dx.doi.org/10.1016/j.ijthermalsci.2015.10.014.
[5] S.I. Abarzhi, Review of theoretical modeling approaches of Rayleigh–Taylor instabilities and turbulent mixing, Phil. Trans. R. Soc. A 368 (2010) 1809–1828.
[6] G. Boffetta, A. Mazzino, S. Musacchio, L. Vozella, Kolmogorov scaling and intermittency in Rayleigh–Taylor turbulence, Phys. Rev. E 79 (2009) 065301–065309.
[7] W.H. Cabot, A.W. Cool, Reynolds number effects on Rayleigh–Taylor instability with possible implications for type-ia supernovae, Nat. Phys. 2 (2006) 562–568.
[8] Q. Zhou, Temporal evolution and scaling of mixing in two-dimensional Rayleigh–Taylor turbulence, PhysFluild 25 (2013) 08510701–08510717.
[9] D. Furihata, A stable and conservative finite difference scheme for the Cahn–Hilliard equation, Numer. Math. 87 (2001) 675–699.
[10] E.V.L. de Mello, O.T. da Silveira Filho, Numerical study of the Cahn–Hilliard equation in one, two and three dimensions, Physica A 347 (2005) 429–443.
[11] H.G. Lee, J. Kim, A second-order accurate non-linear difference scheme for the N-component Cahn–Hilliard system, Physica A 387 (2008) 4787–4799.
[12] H.G. Lee, J.-W. Choi, J. Kim, A practically unconditionally gradient stable scheme for the N-component Cahn–Hilliard system, Physica A 391 (2012) 1009–1019.
[13] J. Kim, A numerical method for the Cahn–Hilliard equation with a variable mobility, Commun. Nonlinear Sci. Numer. Simul. 12 (2007) 1560–1571.
[14] J. Kim, K. Kang, J. Lowengrub, Conservative multigrid methods for Cahn–Hilliard fluids, J. Comput. Phys. 193 (2004) 511–543.
[15] 30, S.M. Choo, S.K. Chung, Conservative nonlinear difference scheme for the Cahn–Hilliard equation, Comput. Math. Appl. 36 (1998) 31–39.
[16] N. Talat, B. Mavrič, V. Hatić, S. Bajt, B. Šarler, Phase field simulation of Rayleigh–Taylor instability with a meshless method, Eng. Anal. Bound. Elem. 87 (2017) (2018) 78–89, http://dx.doi.org/10.1016/j.enganabound.2017.11.015.
[17] Y. Zhou, W.H. Cabot, B. Thornber, Asymptotic behavior of the mixed mass in Rayleigh – Taylor and Richtmyer – Meshkov instability induced flows, 2016, 052712, http://dx.doi.org/10.1063/1.4951018.

[18] H. Huang, M. Sukop, X.Y. Lu, Multiphase Lattice Boltzmann Methods Theory and Application, Vol. 1, John Wiley and Son, West Sussex, UK, 2015.
[19] A.A. Mohammed, Lattice Boltzmann Method: Fundamentals and Engineering Applications with Computer Codes, Springer, 2012.
[20] S.M. Choo, S.K. Chung, K.I. Kim, Conservative nonlinear difference scheme for the Cahn–Hilliard equation—II, Comput. Math. Appl. 39 (2000) 229–243.
[21] D. Sharp, An overview of rayleigh-taylor instability, in: Physica. 12D, north-Holland, Amsterdam, 1984, pp. 3–18.
[22] X. He, R. Zhang, S. Chen, G.D. Doolen, On the three-dimensional Rayleigh – Taylor instability, Phys. Fluids 1143 (1999) http://dx.doi.org/10.1063/1.869984.
[23] V.G. Danilov, Averaging under Rayleigh–Taylor instability and density mushy region generation, Eur. J. Mech. B Fluids 74 (2019) 152–158, http://dx.doi.org/10.1016/j.euromechflu.2018.11.003.
[24] He, S. Chen, R. Zhang, A lattice Boltzmann scheme for incompressible multiphase flow and its application in simulation of Rayleigh–Taylor instability, J. Comput. Phys. 663 (1999) 642–663, [Online]. Available: http://www.ingentaconnect.com/content/ap/cp/1999/00000152/00000002/art06257.
[25] Y. Zhou, W.H. Cabot, Time-dependent study of anisotropy in Rayleigh–Taylor instability induced turbulent flows with a variety of density ratios, Phys. Fluids 084106 (2019) http://dx.doi.org/10.1063/1.5110914.
[26] J.T. Waddell, C.E. Niederhaus, J.W. Jacobs, Experimental study of Rayleigh–Taylor instability: Low atwood number liquid systems with single-mode perturbations, Phys. Fluids 13 (5) (2001) 1263–1273, http://dx.doi.org/10.1063/1.1359762.
[27] A. Banerjee, M.J. Andrews, 3D simulations to investigate initial condition effects on the growth of Rayleigh – Taylor mixing, Int. J. Heat Mass Transfer 52 (17–18) (2009) 3906–3917.
[28] J. Waltz, T.A. Gianakon, A comparison of mix models for the Rayleigh – Taylor instability, Comput. Phys. Comm. 183 (1) (2012) 70–79.
[29] H. Geun, J. Kim, Numerical simulation of the three-dimensional Rayleigh – Taylor instability, Comput. Math. Appl. 66 (8) (2013) 1466–1474.
[30] S. Roy, L.K. Mandal, M. Khan, M.R. Gupta, Combined effect of viscosity, surface tension and compressibility on Rayleigh–Taylor Bubble growth between two fluids, J. Fluids Eng. 136 (9) (2014) 091101.
[31] Y. Zhou, T.T. Clark, D.S. Clark, S.G. Glendining, M.A. Skinner, C.M. Hutington, O.A. Huricane, A.M. Dimits, B.A. Remington, Turbulent mixing and transition criteria of flows induced by hydrodynamic instabilities, Phys. Plasmas 080901 (August) (2019) http://dx.doi.org/10.1063/1.5088745.
[32] H.G. Lee, K. Kim, J. Kim, On the long time simulation of the Rayleigh–Taylor instability, Internat. J. Numer. Methods Engrg. 85 (13) (2011) 1633–1647.
[33] H. Ding, P.D.M. Spelt, C. Shu, Diffuse interface model for incompressible two-phase flows with large density ratios, J. Comput. Phys. 226 (2) (2007) 2078–2095.
[34] J.L. Guermond, L. Quartapelle, A projection FEM for Variable Density incompressible flows, J. Comput. Phys. 165 (1) (2000) 167–188.
[35] G. Tryggvason, Numerical simulations of the Rayleigh–Taylor instability, J. Comput. Phys. 75 (2) (1988) 253–282.